Title

Organic synthesis on Mars by electrochemical reduction of CO2

Journal

Science Advances, 4(10)

ISSN

2375-2548

Authors

Steele, A

Benning, LG

Wirth, R

et al.

Publication Date

2018-10-05

DOI

10.1126/sciadv.aat5118

Peer reviewed

SPACE SCIENCES

Organic synthesis on Mars by electrochemical reduction of CO_2

A. Steele[1]*, L. G. Benning[2,3,4], R. Wirth[2], S. Siljeström[5], M. D. Fries[6], E. Hauri[7†], P. G. Conrad[1], K. Rogers[8], J. Eigenbrode[9], A. Schreiber[2], A. Needham[10], J. H. Wang[7], F. M. McCubbin[6], D. Kilcoyne[11], Juan Diego Rodriguez Blanco[4,12]

The sources and nature of organic carbon on Mars have been a subject of intense research. Steele *et al.* (2012) showed that 10 martian meteorites contain macromolecular carbon phases contained within pyroxene- and olivine-hosted melt inclusions. Here, we show that martian meteorites Tissint, Nakhla, and NWA 1950 have an inventory of organic carbon species associated with fluid-mineral reactions that are remarkably consistent with those detected by the Mars Science Laboratory (MSL) mission. We advance the hypothesis that interactions among spinel-group minerals, sulfides, and a brine enable the electrochemical reduction of aqueous CO_2 to organic molecules. Although documented here in martian samples, a similar process likely occurs wherever igneous rocks containing spinel-group minerals and/or sulfides encounter brines.

INTRODUCTION

The provenance and synthesis mechanisms of abiotic organic carbon phases on Mars are critical to discerning the planet's habitability potential. Both robotic missions to Mars and analyses of martian meteorites have yielded clues as to the presence of volatile and refractory organic compounds in martian rocks (*1*–*7*). Steele *et al.* (*7*) reviewed the possible synthesis mechanisms for organic carbon in martian rocks and advanced the hypothesis that there are four separate potential synthesis pathways for its provenance: impact generated, impact induced, primary igneous, or secondary hydrothermal. There is an inventory of organic carbon in the Tissint meteorite (*7*, *8*) that is not associated with the presence of a carbonate phase, nor is it igneous in origin. The precise mechanism of formation of such an organic carbon pool remains unclear.

Here, we report on the analysis of organic phases associated with titano-magnetite, magnetite, pyrite, and pyrrhotite in three martian meteorites, two of which are falls (Nakhla and Tissint) and one of which is a find [North West Africa (NWA) 1950] (*9*–*11*). In the case of Nakhla, there are secondary martian carbonate and clay phases (including saponite and serpentine) in cracks within the meteorite (*10*, *12*, *13*), while Tissint shows evidence of minimal secondary alteration processes (*14*). In NWA 1950, carbonates have been shown to be of terrestrial origin (*11*, *15*), although an indigenous macromolecular carbon (MMC) phase has been documented in this meteorite (*1*).

[1]Carnegie Institution for Science, Geophysical Laboratory, Washington, DC 20015, USA. [2]German Research Centre for Geosciences, GFZ, Telegrafenberg, 14473 Potsdam, Germany. [3]Department of Earth Sciences, Free University of Berlin, 12249 Berlin, Germany. [4]School of Earth and Environment, University of Leeds, Leeds LS2 9JT, UK. [5]RISE Research Institutes of Sweden, Bioscience and Materials/Chemistry, Materials and Surfaces, Box 5607, 114 86 Stockholm, Sweden. [6]NASA, Johnson Space Center, Houston, TX 77058, USA. [7]Department of Terrestrial Magnetism, Carnegie Institution of Washington, 5241 Broad Branch Rd, Washington, DC 20015, USA. [8]Earth and Environmental Sciences, Rensselaer Polytechnic Institute, 110 8th Street, Troy, NY 12180, USA. [9]NASA Goddard Space Flight Center, Greenbelt, MD 20771, USA. [10]USRA–Science and Technology Institute, 320 Sparkman Drive, Huntsville, AL 35805, USA. [11]Advanced Light Source, 1 Cyclotron Road, MS 7R0222, LBNL, Berkeley, CA 94720, USA. [12]ICRAG, Department of Geology, Trinity College Dublin, Dublin 2, Ireland.
*Corresponding author. Email: asteele@carnegiescience.edu
†Deceased.

RESULTS

Figure 1 shows light and confocal Raman imaging spectroscopy (CRIS) images of the features analyzed in NWA 1950 (Fig. 1, A and B), Nakhla (Fig. 1, C and D), and Tissint (Fig. 1, E to H). The dark feature in the 3D CRIS map in NWA 1950 (Fig. 1B) reveals predominantly titano-magnetite and MMC, as previously documented (*1*). The MMC is intertwined within a network of conglomerated smaller titano-magnetite crystals (Fig. 1B). Similar to Nakhla (Fig. 1, C and D), transmission and reflected light microscopy images reveal two titano-magnetite grains, one broaching the surface (red arrows) and one below the surface of the thin section (not apparent at the surface in Fig. 1C), in an area of mesostasis (red box) (*16*). Last, CRIS mapping of a dark phase within maskelynite in the Tissint meteorite revealed the presence of titano-magnetite, pyrite, and MMC (Fig. 1, E to H). All of these observations highlight the occurrence of MMC closely associated with titano-magnetite in all three meteorites from CRIS observations.

High-resolution transmission electron microscopy (TEM) images of these titano-magnetite/MMC associations (Fig. 2), which followed FIB extractions from the areas shown in Fig. 1, revealed that, in Nakhla, the titano-magnetite is surrounded by pyroxene, K-feldspar, and cristobalite (titano-magnetite, bright contrast; Fig. 2, A to D). Detailed images (Fig. 2, B to D) reveal that the titano-magnetite grain shows a comb-like pattern etching into the grain along exsolution lamellae (Fig. 2, C and D). The titano-magnetite lamellae are closely interlinked with an amorphous carbon-rich phase [based on energy-dispersive x-ray (EDX) analyses labeled MMC in Fig. 2, C and I, and CRIS mapping in Fig. 2M] that does not show any diffraction contrast (fig. S1). Elemental x-ray maps collected using the Kα-line x-ray intensities of Fe, Ti, Cl, Si, C, N, and O (Fig. 2, E to K) indicate that the intact areas are Ti rich, compared with the iron-rich material that appears to have been altered, leaving an amorphous Fe, Al, Si, Ti, N, Cl, O, and MMC-rich region emplaced between the Ti-rich areas of the titano-magnetite grain. Figure 2L is a composite x-ray map of the spatial associations among Fe, Ti, and Cl in this area, highlighting areas of Fe and Cl correlation as well as the interplay of Ti-rich and Ti-poor domains within the titano-magnetite grain. CRIS mapping of the same area confirmed the correlation between titano-magnetite and MMC in this FIB section (Fig. 2M). Combining the CRIS data with EDX mapping shows that the amorphous MMC

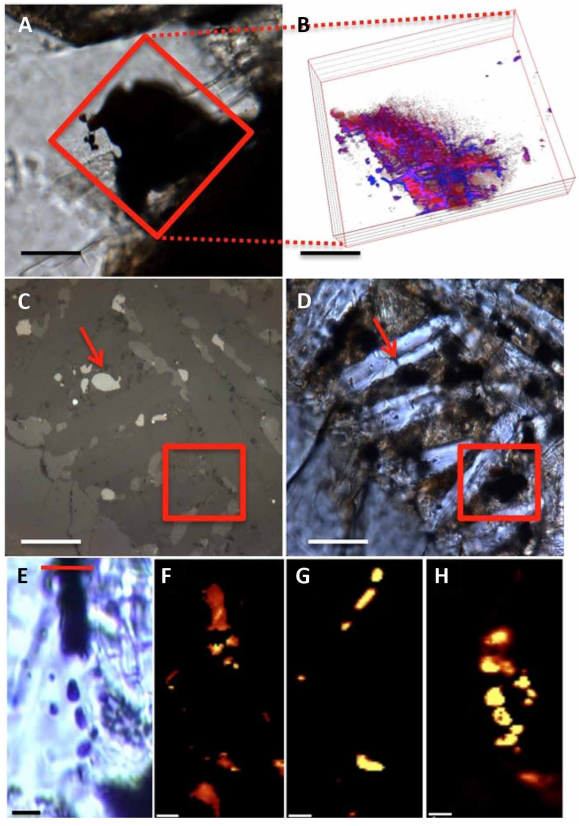

Fig. 1. Light and CRIS of the relationship between magnetite and MMC in the meteorites studied. (**A**) Transmitted light microscopy image of a darkened area within maskelynite, entrained in the subsurface to the thin section in NWA 1950 (scale bar, 100 μm). The red box indicates the area for three-dimensional (3D) mapping by CRIS. (**B**) A 3D depth profile composite CRIS image of magnetite (red) and MMC (blue) (slices are 2 μm apart) from the area denoted by the red box in (A) (scale bar, ~60 μm). (**C** and **D**) The same area of Nakhla mesostasis imaged in transmission and reflection showing a magnetite grain beneath the surface of the section (marked by red arrows) (scale bars, 20 μm). (**E**) Transmitted light image of a magnetite-rich area (dark vertical band) in the Tissint meteorite [scale bar, 20 μm; red line on top delineates the area where a focused ion beam (FIB) section was removed for analyses; see Fig. 4]. (**F** to **H**) CRIS imaging maps taken at 8 μm into the surface of the thin section and depth profile of the feature shown in (A); (F) magnetite, (G) pyrite, and (H) MMC.

contains C, Cl, O, N, Al, Mg, Mn, and Si (Fig. 2M). The chemical correlation between Fe and Cl in Fig. 2L hints at the formation of $FeCl_2$ from this analysis, although the lack of lattice fringes in this material indicates that it is amorphous. These phases are very similar to the previously analyzed "rust phases" in Nakhla and were deemed to be a preterrestrial alteration phase that was heated during Earth entry. These rust phases have been shown to contain Fe, Si, K, and Cl and are characterized by Si-to-Fe ratios varying over a 1- to 10-μm range (*13*, *17*, *18*).

Similar titano-magnetite phases are documented in both Tissint (Figs. 3, A to J, and 4) and NWA 1950 (Fig. 3, K to M). In Tissint, titano-magnetite laths (Fig. 3, C to J) and pyrrhotite grains (Fig. 3L) are both cracked and contain MMC within these cracks. Furthermore, the edges of the titano-magnetite and pyrrhotite grains bordering the MMC-bearing cracks also show the presence of chlorine in EDX analyses. The presence of chlorine in this context indicates similar but potentially less-extensive fluid flow and alteration processes to those described above for Nakhla (Fig. 2). Nano–secondary ion mass spectrometry (nanoSIMS) analyses of hydrogen isotopes in the carbon-rich phases associated with similar alteration cracks in titano-magnetite laths in the Tissint meteorite (Fig. 3, N and O) result in an average δD of ~3600 ± 1000‰ (per mil). This value indicates that the hydrogen associated with the MMC in the Tissint meteorite is of martian crustal origin and arises from a fluid pool that equilibrated with the martian atmosphere (*19*, *20*). The hydrogen isotopes (δD) of MMC in both Nakhla and NWA 1950 are 219 ± 60‰ and 98 ± 20‰, respectively, in areas that correlate to ^{13}C (fig. S4). These values exclude a terrestrial carbon contaminant source (see the Supplementary Materials for a discussion on terrestrial contamination) but are consistent with formation from a martian magmatic water source (*19*, *21*). Therefore, the Tissint meteorite appears to have incorporated atmospheric deuterium dissolved in near-surface brine, while the Nakhla and NWA 1950 MMC formed from a brine drawing from a magmatic source, as described by McCubbin *et al.* (*22*).

Further evidence of the nature of the organic phases in the Tissint meteorite comes from high-resolution TEM and scanning transmission x-ray microscopy (STXM) analyses (Fig. 4A) of a FIB section of the magnetite-rich inclusion shown in Fig. 1E. The low-magnification TEM image (Fig. 4A) shows the inclusion surrounded by the host maskelynite, but with the interface delineated by a series of empty, rounded, bubble-like features and with additional voids inside the inclusion (white arrows in Fig. 4A). The lack of such features in the matrix and the presence of Pt nanoparticles inside the bubbles/voids indicate Pt deposition during the FIB milling. This illustrates that these bubbles/voids are not a product of sample preparation but are indigenous to the Tissint meteorite. EDX and SAED analyses (figs. S2 and S3, and table S1) confirmed that the inclusion contained the following complex mineral phase assemblage: anhydrite (labeled 1 in Fig. 4A), magnetite (labeled 2), Ni-containing pyrrhotite (labeled 3), nanocrystalline mix of magnetite and calcium-aluminum silicates (labeled 4), and a rim of sheet-like alumino-silicate phases (labeled 5 in Fig. 4A, but see also figs. S2 and S3). The presence of magnetite was confirmed in both areas 2 and 4 (Fig. 4A) by EDX and SAED (fig. S3). Magnetite in area 4 is nanophase and associated with an amorphous phase containing primarily Si, Al, and Cl. Of interest is the ribbon-like rim (marked 5 in Fig. 4A), as it also shows the presence of bubbles in some places (see also figs. S2 and S3), primarily along the base of the inclusion (fig. S2C). High-resolution TEM images of the mineral phases in this ribbon/rim revealed d-spacings corresponding to a sheet silicate, tentatively identified as a montmorillonite-like clay formed from fluid-rock interaction (table S1). The magnetite- and pyrrhotite-rich areas of the inclusion were also confirmed through STXM mapping at the Fe-L3 edge (708.62 eV; Fig. 4B), while the corresponding STXM map collected at the C-K edge at 284.9 eV reveals a carbon hot spot (Fig. 4C), corresponding to the magnetite- and pyrrhotite-rich areas. The STXM C-K edge spectrum of this hot spot area [Fig. 4D, spectrum (i)] contains multiple peaks, indicating a complex carbon-rich composition. The major peaks can be attributed to the following carbon functionalities: 284.9 eV (aromatic olefinic rich), 286.4 eV (vinyl-keto groups), 287.2 eV (enol groups), and 288.56 eV (carboxyl groups), with the star demarking a possible shoulder peak at 288.56 eV that may represent a small aliphatic component (*23*). In addition, another STXM C-K edge spectrum acquired from a second inclusion in Tissint [spectrum labeled (ii) in Fig. 4D] shows a similar pattern to spectrum (i) (in Fig. 4D), but with slightly different peak ratios and the presence of a peak corresponding to the C–N=C functional group of nitrogen in a six-membered ring (*24*). These STXM spectra confirm our findings

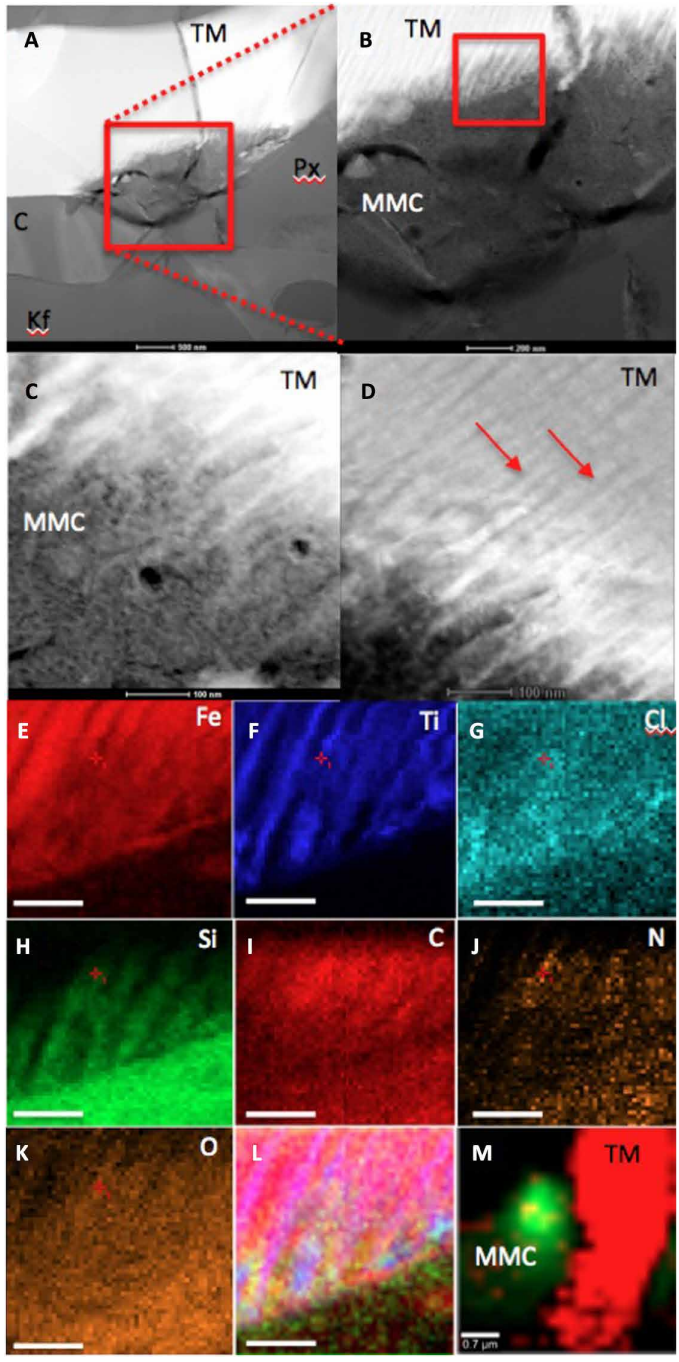

Fig. 2. High-resolution TEM analysis of magnetite and MMC features within the Nakhla meteorite. (**A** to **D**) High-angle annular dark-field (HAADF) TEM images showing (A) a Nakhla titano-magnetite (TM) grain extracted through FIB milling from the area marked with a red box in Fig.1 (C and D). The grain is surrounded by pyroxene (Px), K-feldspar (Kf), and cristobalite (C) (scale bar, 500 nm). (B) A higher-magnification image of the red boxed area in (A), showing evidence of corrosion with a comb-like etching pattern into the TM grain (TM; scale bar, 200 nm). (C) A higher-magnification and high-contrast image of the area denoted by the red box in (B), with the titanium-rich exsolution lamellae in the TM corroded grain visible (red arrows; scale bar, 100 nm). (D) Area showing the interaction with TM exsolution lamellae and the surrounding matrix; the titanium-rich lamellae are highlighted with red arrows; EDX and selected-area electron diffraction (SAED) analyses of this matrix revealed a carbon-rich but amorphous (no diffraction contrast detected during tilting of the sample) assemblage (MMC; scale bar, 100 nm). (**E** to **K**) X-ray intensity maps of the exsolution features from the red box in (B), showing the distribution and associations between (scale bars, 100 nm). (E) Iron, (F) titanium, (G) chlorine, (H) silicon, (I) carbon, (J) nitrogen, and (K) oxygen, while (**L**) is a three-color composite map of Fe (red), Ti (blue), and Cl (green) to show the link between the corrosion of the TM grain and a chlorine-rich brine. (**M**) Composite CRIS map of the FIB section after TEM analysis showing titano-magnetite (red) and MMC (green), confirming the presence of MMC before and after analysis by TEM [note that map (M) is rotated and at a lower magnification compared with the x-ray maps in (A) to (L) and fig. S1; scale bar, 0.7 μm].

from the MMC spectra found by CRIS and show an amorphous polyaromatic material with no graphitic domains (a characteristic peak at 290.1 eV indicative of graphite is absent in the STXM spectra). The presence of carbon-nitrogen functional groups was cross-confirmed by scanning the same area as Fig. 4D [spectrum (i)] at the STXM N-K edge (390 to 440 eV; Fig. 4D). The results reveal the presence of a shoulder at 398.5 eV, again indicative of a C–N=C functional group with nitrogen in a six-membered ring (pyridine) and pyrollic functional groups at 402.5 eV. These observations are consistent with the elemental analysis of the MMC in Nakhla (Fig. 2J) that showed a clear correlation between nitrogen and carbon in the alteration features analyzed. However, with the STXM analyses, we can extend this to infer the provenance of nitrogen to aromatic functional groups (*24*, *25*).

In an attempt to further test the STXM results and to gain additional information on the nature of organic carbon found in this study, we also carried out time-of-flight secondary ion mass spectrometry (ToF-SIMS) analyses on fresh fracture surfaces of Tissint, Nakhla, and NWA 1950 meteorites [Fig. 5 (Tissint), and extended in figs. S5 (Tissint), S6 (NWA 1950), and S7 (Nakhla), as well as table S2]. The data reveal the presence of a complex chemical mixture containing Cl^-, S^-, SO_3^-, CN^-, CNO, $COOH^-$, C_2S^-, FeO_2^-, $FeCl^-$, ClO^-, and ClO_4^- and confirm the presence of a plethora of organic functional groups, including $COOH^-$, CH_2O^-, CN^-, C_3N^-, $C_2N_3^-$, C_5N^-, C_7N^-, CNO^-, CS^-, C_2S^-, and $C_4H_4S^-$. Apart from the nitrogen-containing species, the alkyl, aromatic, and in particular, sulfur-containing species (i.e., $C_4H_4S^-$, thiophene fragment) of these analyses are a close chemical match to similar analyses performed on Mars using the Sample Analysis at Mars (SAM) instrument in Mojave drill samples and by SAM-like experiments in the laboratory on the Tissint meteorite (*2*). In the ToF-SIMS analyses, these species map to areas of the sample that also contain C^-, OH^-, FeO_2^-, $FeCl^-$, S^-, Cl^-, SO_3^-, and interestingly, ClO^- and ClO_4^- (see the red box in the Cl^- image of Fig. 5). The overlap between the maps of organic carbon and Cl^-, S^-, $FeCl^-$, and FeO_2^- in certain areas of the sample further strengthens our hypothesis that there is a clear relationship between the organic material (MMC) and a Cl-rich brine that interacted to produce common alteration phases. The presence of ClO^- and ClO_4^- within chlorine- and organic-bearing areas strongly suggests the presence of perchlorate-like compounds in these meteorites. Perchlorates have been detected both on Mars by the Phoenix and MSL missions and within other martian meteorites (*3*, *26*, *27*).

DISCUSSION

Organic synthesis mechanism

The spatial relationships between organic carbon, nitrogen, and sulfur compounds and their intimate link to spinel-group minerals (i.e., titano-magnetite), sulfides, and their alteration products and

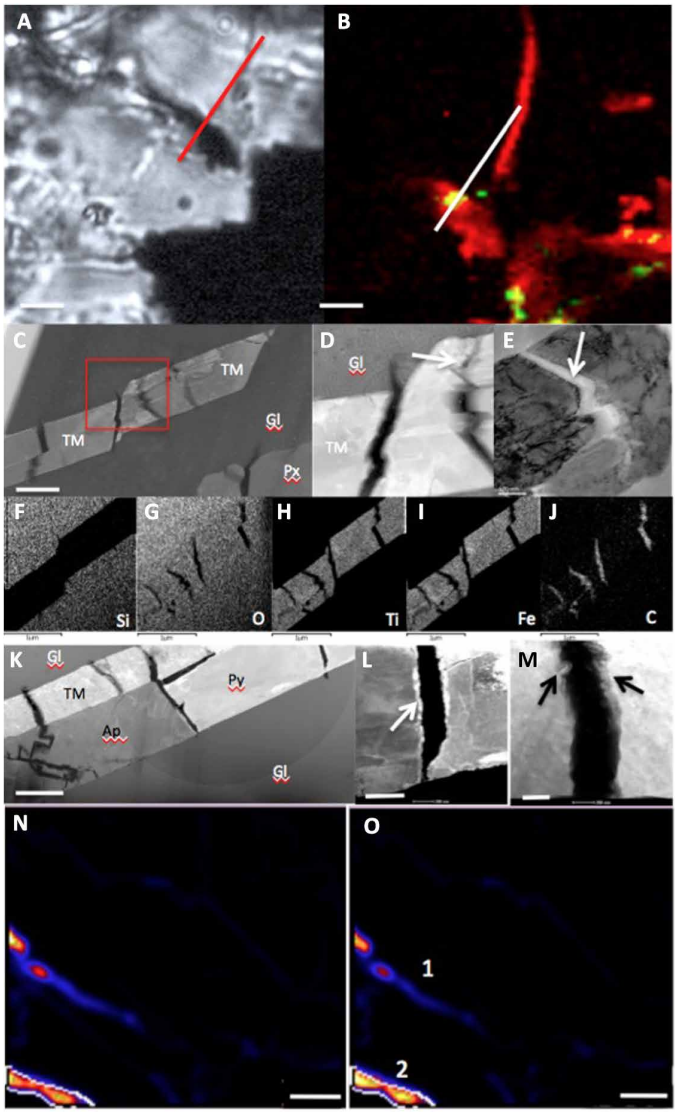

Fig. 3. TEM and hydrogen isotopic analysis of MMC-rich areas in the Tissint meteorite. (**A**) Light microscopy image of a TM lath within maskelynite in the Tissint meteorite (dark area across the line denotes the area from which the FIB section was extracted). Scale bar, 3 μm. (**B**) Composite CRIS map showing TM in red and MMC in green; the white line corresponds to the red FIB line in (A). Scale bar, 3 μm. (**C** to **E**) TEM HAADF images of the extracted FIB section shown in (A) and (B), illustrating that the TM lath is cracked along its length. Scale bars, 500 nm (C) and 100 nm (D and E). (D) A closeup image of the red box in (C), showing two of the cracks and evidencing that the edge of the cracks are corroded (white arrow). (E) Cracks filled with MMC as documented in the EDX maps in (F) to (J). (**F**) Silicon, (**G**) oxygen, (**H**) titanium, (**I**) iron, and (**J**) carbon. Scale bars, 1 μm (F to J). (**K** to **M**) HAADF image of an inclusion assemblage in NWA 1950. The high-resolution images and analyses of the FIB section revealed that TM, and in this case, pyrrhotite and apatite laths are also cracked, and we know from the CRIS mapping shown in Fig. 1B that the magnetite is intimately interlinked in NWA 1950 with MMC. Scale bars, 2 μm (K), 300 nm (L), and 200 nm (M). Crack in pyrrhotite with the edges lined with deposited magnetite nanocrystals (area of high brightness lining the crack marked with a white arrows). (M) Close-up of the TM grains again showing evidence of corrosion along the edges of the cracks in the grains (arrows). (**N**) C^{13}, nanoSIMS map of a different TM lath in the Tissint meteorite that had previously been confirmed by CRIS to contain MMC. Scale bar, 5 μm. (**O**) Deuterium map of the same area as in (N); area 1 recorded a δD of 2252 ± 392‰ and area 2 recorded a δD of 4536 ± 1113‰, scale bar, 5 μm.

textures, as well as the presence of chloride and oxychlorine species, require a synthesis mechanism that is parsimonious with the presence of all of these molecules. The implications of the chemical associations shown in these meteorites are that a Cl-rich fluid (brine) reacted with magnetite, pyrrhotite, pyrite, and titano-magnetite grains to initiate a galvanic cell. This is starkly illustrated in the case of Nakhla where the Fe-rich, Ti-poor lamellae appear to be corroded, leading to the formation of pore space between the relatively intact Ti-rich, Fe-poor lamellae. This is concordant with Nakhla's extensive evidence of secondary fluid alteration by a brine that was intermittently saturated with bicarbonate while resident on Mars (*10*, *22*, *28*). Together with our current findings (e.g., Fig. 2 and fig. S1), this suggests that a halide/bicarbonate brine was the source of the electrolyte for the apparent galvanic corrosion features in the titano-magnetite grain evidenced in Fig. 2. In this scenario, the Ti-rich lamellae are cathodic compared with the Fe-rich lamellae (anodic), with subsequent dissolution of the Fe-rich phase. Given the context of the organic chemistry within and adjacent to apparent mineral alteration textures, the obvious question that arises is: Can there be an electrochemical explanation for the presence of organic phases and perchlorates based on the fluid-alteration processes apparent in these samples? A number of organic species have been shown to be produced during the electrochemical reduction of CO_2 (ERC) linked to the hydrogen evolution reaction (HER) and include H_2, CH_4, HCOOH, CO, C_2H_4, C_2H_6, C_2H_5OH, and CH_4O (*29*–*31*). Both the ERC and HER reactions are known to take place at the cathode that in this case would be the intact Ti-rich lamellae, and there appears to be a spatial correlation between C and N distributions between the Ti-rich laths (Fig. 2, F, I, and J). The STXM spectra shown in Fig. 5D, in addition to a dominant olefinic aromatic peak at ~285 eV, reveal a range of carbon-oxygen functional groups, including C–O, C=O, and COOH, which is certainly consistent with the expected products of ERC (*29*–*31*). The important factor in ERC that determines the speciation of products is the electrode material (*29*). For instance, in the apparent corrosion rim highlighted in fig. S1, Ti, Fe, Mn, Si, and Al were all present, and Azuma *et al.* (*29*) showed that these metals would in general produce a combination of H_2 > CO > HCOOH > CH_4 through the ERC and HER reaction mechanisms (*32*–*34*). Thus, the critical factors become the galvanic potential and current—as well as the streaming potential, given the geometry of the mineral alteration lamellae—that are induced across the boundaries between magnetite, titano-magnetite, and sulfides and whether these potentials are sufficient for ERC and HER reactions to take place. It has been shown that titano-magnetite, magnetite, pyrite, and pyrrhotite all produce enough electrochemical energy at low pH to drive the HER at the cathodic site, and in some cases (with added voltage), to inefficiently, but directly, reduce CO_2 (*32*–*35*). Both the HER and ERC have similar potential ranges and compete at the cathode to provide an environment where electrochemical energy and catalysis from released ions combine to produce organic compounds from the reduction of aqueous CO_2. In natural systems, magnetite would serve as a source for catalytic ferrous ions that may facilitate reduction of CO_2; however, there is very little research on this effect in natural materials, and natural systems are intrinsically more complex than their simplified experimental counterparts (*32*). For example, Al, Si, Ti, Mn, V, Cr, and Ni—trace metals common to the natural systems studied here—are all possible electrode materials for ERC (*29*), thus affecting the potential and organic speciation of the ERC reaction in these systems. Furthermore, diverse conditions,

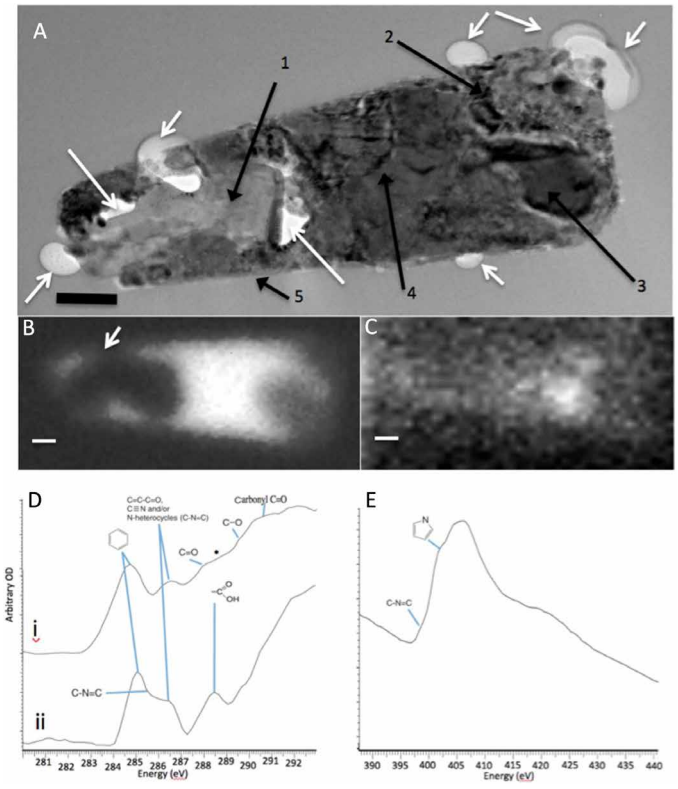

Fig. 4. TEM imaging and soft transmission x-ray analysis of MMC within an inclusion of the Tissint meteorite. (**A**) Bright-field TEM image of a FIB section from the Tissint meteorite milled from the area analyzed by CRIS. The image reveals a highly complex inclusion. White arrows indicate bubbles protruding into the surrounding maskelynite matrix or void space inside the inclusion. Black arrows point to specific mineral phases identified by high-resolution imaging and EDX and SAED analyses (figs. S2 and S3) corresponding to (1) anhydrite, (2) magnetite and carbon, (3) Ni-containing pyrrhotite, (4) nanocrystalline multiphase magnetite and calcium-aluminium silicate phases, and (5) rim of sheet silicate–like aluminosilicate, probably montmorillonite (scale bar, 150 nm). (**B**) STXM map of Fe at 708.62 eV showing the iron-rich area of the inclusion (in white), including the area around the anhydrite grain and the bubble projecting into the glass matrix (arrow). (**C**) STXM map at the C-K edge at 284.9 eV showing a hot spot of aromatic carbon corresponding to pyrrhotite and magnetite (areas 2 and 3) shown in (A) (lighter shade shows greater concentration). Scale bars, 200 nm. (**D**) STXM spectrum of two inclusions from Tissint: (i) hot spot area in (C), showing the presence of peaks at 284.9, 286.4, and 288.56 eV, with a star demarking a possible shoulder peak at 288.56 eV; (ii) peaks from another inclusion containing many of the same functional groups as in (i) but also a shoulder at 285.6 eV, which is possibly indicative of 400 eV and pyrrole functionality at 405 eV. (**E**) STXM N-K edge spectrum from the same inclusion as spectrum (i) in (D), confirming the presence of C–N=C functionality at 400 eV and a pyrrole group at 405 eV. OD, optical density.

such as the presence of different ionic species or changes in pH, temperature, and pressure, as well as electrode distance, morphology, size, composition, and electrolyte concentrations, would all be important to drive these reactions (*36*). In addition, the proximity of anode and cathode is directly related to the electrochemical charge density available for ERC (*36*). In the system shown in Figs. 2 and 3, the geometry of adjacent mineral surfaces and alteration lamellae define the diffusion boundaries between the anode and cathode, which are in the nanometer range, as well as the spatial scale of the fluid flow, which is in the submicron range. This geometry is on par with microfluidic systems, and in recent years, there has been a revolution in microfluidic electrochemical reactors for organic synthesis relying on a very small gap between anode and cathode, and in some instances, overlapping anode-cathode systems. To quote Zimmermann and Limberg (*37*), one advantage of this is that "…very high field strengths can be produced from only a small voltage difference due to the inverse proportionality of electric field strength to the gap separating the voltages driving the reactor…." Such a phenomenon has given rise to a whole new field of coupled organic synthesis reactions using electrosynthesis in miniaturized flow systems to undertake a range of reactions, including aldol, peptide synthesis, nitration, amide synthesis dehydration, and phase transfer (*38*). Additional electrochemical pathways also include the reduction of nitrate and nitrite, both of which have been found in meteorites and martian regolith, by pyrite and pyrrhotite to ammonia (*39*). Therefore, considering the association of nitrogen with Ti and Fe in Fig. 2J (red cross) and the speciation of nitrogen from STXM and ToF-SIMS data (Figs. 4 and 5), it is possible that electrochemical reduction took place from either nitrides or dinitrogen to ammonia in a manner similar to that observed with experimental electrochemical systems (*40*). Pyrrhotite can act to reduce nitrogen to ammonia at redox conditions consistent with the pyrite-pyrrhotite-magnetite mineral assemblage, and ammonia can then react with CO, CO_2, or CH_4 to form organic nitrile groups, and thus the functionality observed in these analyses (*41*).

The prevalence of aromatic carbon and carbon-oxygen functional groups detected by STXM is also noteworthy. It appears that the secondary reaction of the products from ERC has undergone further reactions, such as aqueous Fischer-Tropsch–type synthesis and elongation, methanol-to-hydrocarbon conversions, or Diels-Alder–type reactions of alkenes. In laboratory settings, a soot-like carbon has been shown to build up on galvanic cell electrodes for ERC, to produce an MMC-like phase that is currently poorly characterized, but which is potentially analogous to the MMC described in these analyses (*42*). The STXM spectra (Fig. 4, D and E) of the carbonaceous phase in Tissint bear an uncanny resemblance to the MMC found both in Murchison and in experiments to polymerize formaldehyde, thus possibly indicating a similar mechanism of aromatization from low carbon number compounds to organic matter dominated by aromatic and olefinic groups. Furthermore, once produced, the primary ERC products, CH_4, CO, H_2, NH_3, and HCOOH, would interact with mesoporous amorphous Fe, Ti, and Mn, oxides in a Si- and Al-rich phase, allowing further catalytic transformations. These primary ERC products have also been invoked as critical precursors for alternative abiotic synthesis mechanisms, including hydrothermal synthesis in early Earth vent systems (*43*, *44*), hydrothermal alteration of meteorite parent bodies (*45*), Strecker synthesis (*46*), or Miller-Urey–style spark discharge synthesis of amino acids (*47*). The observations presented here for the martian meteorites call upon electrical charge differences due to galvanic processes in an aqueous medium as the energy that drives organic synthesis processes. These galvanic processes may well occur in systems undergoing aqueous hydrothermal alteration but are critically dependent on the electrochemical potential, geometry, and surface area of minerals that act as complementary anodic and cathodic materials. Although speculated about previously (*48*), the ERC process as a natural abiotic synthesis mechanism would represent a paradigm shift in thinking about abiotic pathways in early life chemistry and begin to explain incongruities between mechanisms that have been observed to have high organic synthesis yields and the associated

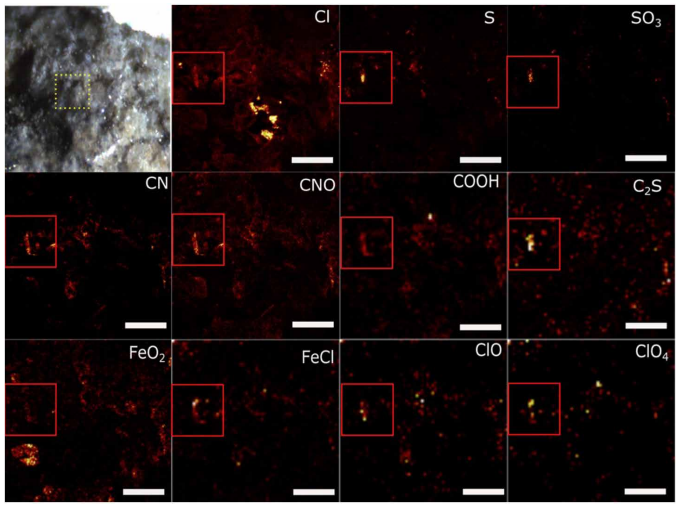

Fig. 5. ToF-SIMS analysis of fresh fracture surface of the Tissint meteorite. The first image is a light microscope image of a fresh fracture surface of the Tissint meteorite, as analyzed within the ToF-SIMS instrument. Individual species are recorded in the top right of the individual images and include Cl^-, S^-, SO_3^-, CN^-, CNO^-, $COOH^-$, C_2S^-, FeO_2^-, $FeCl^-$, ClO^-, and ClO_4^-. The red box in the first ion image of the first row (Cl^-) denotes an area of concentration of many carbon-, nitrogen-, chlorine-, iron-, and sulfur-containing species that are labeled in the top right of the remaining images. Scale bars, 20 μm. See table S2 for absolute peak assignments and fig. S5 for further species maps.

experimental results that fall short of theoretical or observed predictions. For example, in recent years, experimental reactions to generate methane via serpentinization reactions in the laboratory have hit a major hurdle in the production of methane (*49*), in that not enough hydrogen is produced during the weathering of pure olivine. However, subsequent studies have implicated the presence of magnetite as the phase that is most likely to produce excess hydrogen and aid in methane production during serpentinization reactions (*50*). While none of these studies have taken into account the electrochemical reactions described above, they are suggestive of increased availability of hydrogen through the HER via galvanic corrosion processes enhanced by the presence of magnetite. Such a reaction chain would enable abiotic hydrocarbon synthesis reactions to occur wherever igneous provenances interact with brines in systems where the water/rock ratio remains low.

Formation of perchlorate

The presence of hypochlorite (ClO^-) and perchlorate ions (ClO_4^-) found associated with iron corrosion products and organics in all meteorites is a further indicator of electrochemical processes (Fig. 5). Electrochemical techniques are extensively used in an industrial process to generate perchlorates from brines. Furthermore, perchlorates detected in municipal drinking supplies result from electrochemical reactions of manganese oxides with chlorinated drinking water (*51*, *52*). In the case of the corrosion features in the martian meteorites described above, EDX analyses confirm the presence of small amounts of Mn in both the grains and the corrosion products (fig. S1). This stepwise process is initiated with the electrochemical oxidation of sodium chloride to sodium chlorate by an anodic reaction, followed by further electrochemical oxidation of chlorate to perchlorate. This reaction has been shown to be initiated by the use of magnetite electrodes, although the process requires a large overpotential in industrial chemical reactors and has not been previously witnessed in natural samples or municipal drinking water systems (*53*, *54*). However, one interesting aspect to the presence of ClO^- and ClO_4^- in the meteorites is that the potentials needed to generate these species during the electrochemical reactions with a brine are more than sufficient for the HER and ERC reactions (*55*). Thus, the presence of ClO^- and ClO_4^- in the same areas as the corrosion products in the meteorites and organic material indicates that the conditions for organic synthesis from HER and ERC have been met in these systems.

CONCLUSIONS

Indigenous organic phases within Tissint, Nakhla, and NWA 1950 appear to be produced from the interaction of a brine with magnetite, pyrrhotite, and titano-magnetite phases. We posit that the organic phases in these meteorites result from reactions similar to those known to occur during the ERC. While the efficiencies of conversion of a CO_2-containing brine to organic compounds and perchlorate by corrosion of magnetite, titano-magnetite, and sulfides cannot be modeled directly with current data, it is a highly compelling explanation for the co-occurrence of organic phases and perchlorate in this study. The hypothesis developed from our observations on martian meteorites has profound implications for our understanding of other martian phenomena, including the presence of methane in the atmosphere (*56*) and the origin of the refractory organic material in ancient sedimentary rocks found in situ by the SAM instrument (*2*) (survival through ejection and transport to Earth is discussed in the Supplementary Materials). The data presented herein showing chemical and physical details of organics in martian meteorites overlap significantly with analyses by the SAM instrument onboard the Curiosity rover. These two datasets together represent a mutually confirming analysis of the presence and provenance of organic material in martian materials conducted using state-of-the-art analysis tools on two planets. It is the powerful combination of robotic and laboratory analyses that has led to the development of the testable hypothesis presented herein. This hypothesis requires validation by more focused robotic investigation of samples to be returned from Mars, followed by laboratory experimentation and analyses of those returned samples. However, abiotic organic synthesis by ERC offers the most parsimonious explanation of the presence of organics in martian meteorites and the igneous component of martian sedimentary rocks to date (*2*).

The dimensions and heterogeneity of the fluid-mineral interactions apparent in the features analyzed here, together with the observed overlap between anodic and cathodic boundary layers, show that natural systems may support electrochemical, electrocatalytic, and electrosynthetic reactions in what is essentially an environmental nano- or microfluidic device powered by corrosion processes. While found here in martian samples, a similar process would occur wherever igneous rocks encountered brines, and therefore may be a dominant process for the production of organic phases and essential prebiotic molecules and their precursors on early Earth, Europa, and Enceladus.

MATERIALS AND METHODS

Samples

Analyses were conducted on both thin sections and fresh fracture surfaces of the three meteorites in question. Samples of Nakhla were

provided by the Johnson Space Center; those of Tissint were provided by the University of New Mexico and the Natural History Museum, London (C. Smith); and those of NWA 1950 were provided by the Carnegie Institution of Washington.

Light microscopy

Light microscopy imaging was used to define areas of interest for Raman microscopy. Optical imaging was performed with an Olympus BX61 microscope coupled to computer control using Olympus cellSens software. Maps of the samples were prepared using both transmission and reflected light at ×40 and ×100 using the multiple image alignment function of the microscope. These maps were then used to locate areas for CRIS imaging and FIB milling.

Confocal Raman imaging spectroscopy

Raman spectra and images were collected using a Witec α-Scanning Near-Field Optical Microscope that has been customized to incorporate confocal Raman spectroscopic imaging. The excitation source was a frequency-doubled solid-state yttrium-aluminum-garnet laser (532 nm) operating between 0.3- and 1-mW output power (dependent on objective), as measured at the sample using a laser power meter. Objective lenses used included a ×100 Long Working Distance (LWD) and a ×20 LWD, with a 50-μm optical fiber acting as the confocal pinhole. Spectra were collected on a Peltier-cooled Andor electron-multiplied charge-coupled device chip, after passing through an f/4 300-mm focal length imaging spectrometer typically using a grating of 600 lines/mm. The lateral resolution of the instrument was as small as 360 nm in air when using the ×100 LWD objective, with a focal plane depth of ~800 nm.

This instrument is capable of operating in several modes. Typically, 2D imaging and single spectra modes were used during this study. Single spectra mode allows the acquisition of a spectrum from a single spot on the target. Average spectra were produced typically using integration times of 30 s per accumulation and 10 accumulations to allow verification of weak spectral features.

Dependent on whether the sample was a thin section or fresh fracture surface, we used either transmitted or reflected light microscopy to locate the field of interest. Target areas were identified on the thin section in transmitted light. The microscope was then switched to reflected light and refocused to the surface, at which point X, Y, and Z piezos of the stage were reset. Switching back to transmitted light then allowed an accurate measurement of the depth of the feature of interest. The height and width of the field of interest within the light microscopy image were then measured and divided by the lateral resolution of the lens being used, to give the number of pixels per line. The instrument then acquired a Raman spectrum (0 to 3600 cm^{-1} using a grating of 600 lines/mm) at each pixel using an integration time of between 1 and 6 s per pixel. For depth profiles, stack scan mode was used with a depth spacing of 1 μm per scan for a maximum of 16 scans (16 μm) into the surface.

A cosmic ray reduction routine was used to reduce the effects of stray radiation on Raman images, as was image thresholding to reject isolated bright pixels. Fluorescence effects were inhibited by the use of specific peak fitting in place of spectral area sums and by the confocal optics used in this instrument. The effects of interfering peaks were removed by phase masking routines based on multiple peak fits, as compared with standardized mineral spectra. This produced an average spectrum over the number of pixels chosen in the area of interest. In a typical scan at ×100 of a 30-μm^2 area, 100 pixels by 100 pixels were scanned, amounting to 10,000 separate and spatially aligned Raman spectra, from which average spectra from areas of interest were generated to ascertain the presence or absence of a certain peak.

FIB sample preparation

Electron transparent TEM foils were prepared by using the FIB system at GeoForschung Zentrum (GFZ) Potsdam. Details of FIB sample preparation with FIB can be found elsewhere (*57*, *58*).

Transmission electron microscopy

TEM analysis of the FIB-prepared foils was performed with a TECNAI F20 X-Twin transmission electron microscope at GFZ Potsdam. The TEM was operated at 200 keV with a Schottky field emitter as electron source. The TEM is equipped with a Gatan imaging filter (TRIDIEM), a Fishione high-angle annular dark-field detector HAADF, and an EDAX energy-dispersive spectroscopy x-ray analyzer. Electron energy-loss spectra were acquired in diffraction mode at a camera length of 620 mm and an energy dispersion of 0.1 eV per pixel. EEL spectra were processed using the Digital Micrograph software package.

NanoSIMS

Isotopic imaging was performed using the NanoSIMS 50L ion microprobe at the Department of Terrestrial Magnetism, Carnegie Institution of Washington. The selected area (in Fig. 1) of the sample was first presputtered using a 5- to 10-nA Cs beam to remove surface contamination and to sputter down through the sample until the area of interest was reached and exposed; an electron flood gun was used for charge compensation. We then used a 200-pA primary beam of Cs ions focused to a diameter of 400 nm for obtaining isotopic images. Simultaneous detection and imaging of ^{1}H, ^{2}D, and ^{13}C were obtained by rastering the primary beam over areas of 15 μm by 15 μm starting at the surface of the section over the feature shown in Fig. 1 and sputtering down into the section for a distance of ~8 μm. For image acquisition, the sputter crater was divided into 256 pixels by 256 pixels, and beam blanking was not used. Data were recorded as scanning ion images obtained simultaneously on each isotopic mass at a depth of profile of ~2 μm per data acquisition for a total of four data acquisitions. Data were extracted and processed from the ion images using the L'Image software package for PV-Wave written by L. Nittler [Department of Terrestrial Magnetism, Carnegie Institution of Washington (DTM-CIW)]. Data were first collected on an organic standard supplied by L. Nittler and were used to correct the instrument mass fractionation effects. Count rates were corrected for detector dead time (44 ns), and the data were standardized using the series of analysis on several areas of the standard with known isotopic compositions. Additional details of the method can be found in Hauri *et al.* (*59*). Thin section polymer signal was analyzed and corrected = −150‰.

Carbon x-ray absorption near-edge structure spectroscopy

The analysis of organic matter at the size scale of individual inclusions shown in Fig. 3 was difficult and similar to the challenges posed by interplanetary dust particles and returned Comet 81P/Wild2 samples/particles, for example. The most powerful tools for such analyses are STXMs (soft) or scanning transmission x-ray spectrometers. STXMs use Fresnel zone plate optics, providing a theoretical spot size of 30 nm; in optimum cases, smaller structures (approximately 15 nm)

can be resolved. In the present case, the STXM located at beamline 5.3.2 at the Advanced Light Source, Lawrence Berkeley Laboratory, was used for all analyses. The maximum scanning rates for the STXM at beamline 5.3.2 is 12 Hz, with a scanning range of 4000 pixels by 2000 pixels, covering a region up to 20 mm by 4 mm, with a minimum step size of 2.5 nm. Sample position precision during spectra acquisition was better than 50 nm (controlled by laser interferometery). C-, N-, and O-XANES (x-ray absorption near-edge structure spectroscopy) spectra were acquired using a multispectral imaging method. The "stacks" method relied on creating a highly aligned hyperspectral data cube of x by y pixelated images acquired over a range of energies that span a given XANES region. In the fine structure regions of the near edge, the energy step size (ΔE) typically used was 0.1 eV; in the less featured pre- and post-edge regions, energy steps of 1 to 2 eV were sufficient for spectral resolution. C-XANES reveals the presence and abundance of various organic functional groups via the detection of characteristic absorption features in the near-edge (preionization) region of the x-ray absorption spectrum. In general, absorption at the lowest energies (approximately 285.0 eV) is well described by photoexcitation of carbon 1s electrons to low-energy, unoccupied, π0 orbitals of alkenyl and aromatic species (C and H substituted). Carbon substitution with more electronegative atoms (e.g., N and O) results in shifts to higher excitation energies, e.g., 288.5 eV in the case of carboxyl 1s-π0 transitions.

Time-of-flight secondary ion mass spectrometry

ToF-SIMS analyses were performed on fresh fracture surfaces of Tissint, NWA 1950, and Nakhla at a ToF-SIMS V instrument (ION-TOF GmbH, Germany) at the Department of Physics, Chemistry and Biology at Linköping University, Sweden. A focused 2.5-keV Ar cluster beam was rastered over an area of 500 μm by 500 μm at a current of 0.3 to 0.5 nA for ~300 s. The argon cluster sputtering removed any contaminants that might have deposited on the surface of fresh fracture from the laboratory air. The mean size of the Ar clusters was 1500. After cleaning with Ar cluster source, a <150 μm by 150 μm (128 pixels by 128 pixels or 256 pixels by 256 pixels) area centered within the sputtered region was analyzed. The analyses were done with a 30-keV Bi_3^+ beam at a pulsed current of 0.3 to 0.5 pA in high mass resolution mode [bunched mode, $m/\Delta m$ ~5000 to 6000 at m/z (mass/charge ratio) 30, Δl ~ 5 μm]. In addition, spectra collected in high spatial resolution mode (0.05 to 0.1 pA; burst alignment mode, $m/\Delta m$ 100 to 300, Δl < 1 μm) were acquired from the analysis areas. The sample surface was flooded with electrons for charge compensation during the analyses.

The assigned peaks have a deviation of <100 parts per million at a mass range of m/z 0 to 1500 in the high mass resolution mode. All data were saved as raw data files, which make it possible to perform retrospective analysis; that is, additional spectra, ion images, and profiles of the specific masses and regions of interest can be retrieved after the data acquisition is completed.

Figure 5 shows high spatial resolution images of the ion species. Because of the low mass resolution ($m/\Delta m$ ~100 to 300) of this mode, peaks at the same nominal mass cannot be separated. Therefore, covering the same area, mass spectra of high mass resolution ($m/\Delta m$ ~5000 to 6000) but of low spatial resolution were also acquired. The ion images produced from these were compared with high spatial resolution to ensure the same spatial distribution. In most cases, the interesting species were major species at the nominal mass (see tables S2 to S4).

SUPPLEMENTARY MATERIALS

Supplementary material for this article is available at http://advances.sciencemag.org/cgi/content/full/4/10/eaat5118/DC1

Section S1. On the nature of contamination in these analyses.
Section S2. The shock survival of indigenous martian organics.
Fig. S1. Same titano-magnetite grain in Nakhla as imaged and shown in Fig. 2, illustrating the chemical composition of the sample from EDX spectra taken at several points.
Fig. S2. Same inclusion in Tissint as imaged in TEM and shown in Fig. 4A, illustrating the chemical composition of the sample from EDX spectra taken at several points.
Fig. S3. Same inclusion as imaged in Fig. 4A and fig. S2 showing high-resolution TEM images of the measurements of lattice fringe dimensions and SAED patterns from each of the phases shown by blue arrows and reported in Fig. 4A.
Fig. S4. NanoSIMS depth profile analysis of NWA 1950 and Nakhla.
Fig. S5. Supplementary figure to complement Fig. 5 (ToF-SIMS analysis of Tissint); mass assignments are covered in table S2.
Fig. S6. ToF-SIMS analysis of a fresh fracture surface of Nakhla.
Fig. S7. ToF-SIMS analysis of a fresh fracture surface of NWA 1950.
Table S1. Summary of d-space measurements on the areas marked in fig. S3 and the mineral identification from the International Center for Diffraction Data database.
Table S2. This table pertains to Fig. 5 and fig. S5 and summarizes the mass peaks used to make the chemical designations (peak assignments) shown in these images.
Table S3. This table pertains to ToF-SIMS analysis of Nakhla in fig. S6 and summarizes the mass peaks used to make the chemical designations (peak assignments) shown in these images.
Table S4. This table pertains to ToF-SIMS analysis of NWA 1950 in fig. S7 and summarizes the mass peaks used to make the chemical designations (peak assignments) shown in these images.
References (*60*–*68*)

REFERENCES AND NOTES

1. A. Steele, F. M. McCubbin, M. Fries, L. Kater, N. Z. Boctor, M. L. Fogel, P. G. Conrad, M. Glamoclija, M. Spencer, A. L. Morrow, M. R. Hammond, R. N. Zare, E. P. Vicenzi, S. Siljeström, R. Bowden, C. D. K. Herd, B. O. Mysen, S. B. Shirey, H. E. F. Amundsen, A. H. Treiman, E. S. Bullock, A. J. T. Jull, A reduced organic carbon component in martian basalts. *Science*. **337**, 212–215 (2012).
2. J. L. Eigenbrode, R. E. Summons, A. Steele, C. Freissinet, M. Millan, R. Navarro-González, B. Sutter, A. C. McAdam, H. B. Franz, D. P. Glavin, P. D. Archer Jr., P. R. Mahaffy, P. G. Conrad, J. A. Hurowitz, J. P. Grotzinger, S. Gupta, D. W. Ming, D. Y. Sumner, C. Szopa, C. Malespin, A. Buch, P. Coll, Organic matter preserved in 3-billion-year-old mudstones at Gale crater, Mars. *Science* **360**, 1096–1101 (2018).
3. D. P. Glavin, C. Freissinet, K. E. Miller, J. L. Eigenbrode, A. E. Brunner, A. Buch, B. Sutter, P. D. Archer Jr., S. K. Atreya, W. B. Brinckerhoff, M. Cabane, P. Coll, P. G. Conrad, D. Coscia, J. P. Dworkin, H. B. Franz, J. P. Grotzinger, L. A. Leshin, M. G. Martin, C. McKay, D. W. Ming, R. Navarro-González, A. Pavlov, A. Steele, R. E. Summons, C. Szopa, S. Teinturier, P. R. Mahaffy, Evidence for perchlorates and the origin of chlorinated hydrocarbons detected by SAM at the Rocknest aeolian deposit in Gale Crater. *J. Geophys. Res. Planets* **118**, 1955–1973 (2013).
4. C. Freissinet, D. P. Glavin, P. R. Mahaffy, K. E. Miller, J. L. Eigenbrode, R. E. Summons, A. E. Brunner, A. Buch, C. Szopa, P. D. Archer, H. B. Franz, S. K. Atreya, W. B. Brinckerhoff, M. Cabane, P. Coll, P. G. Conrad, D. J. Des Marais, J. P. Dworkin, A. G. Fairén, P. François, J. P. Grotzinger, S. Kashyap, I. L. Ten Kate, L. A. Leshin, C. A. Malespin, M. G. Martin, F. J. Martin-Torres, A. C. McAdam, D. W. Ming, R. Navarro-González, A. A. Pavlov, B. D. Prats, S. W. Squyres, A. Steele, J. C. Stern, D. Y. Sumner, B. Sutter, M. P. Zorzano, Organic molecules in the Sheepbed mudstone, Gale Crater, Mars. *J. Geophys. Res. Planets* **120**, 495–514 (2015).
5. I. P. Wright, M. M. Grady, C. T. Pillinger, Organic materials in a martian meteorite. *Nature* **340**, 220–222 (1989).
6. M. M. Grady, A. B. Verchovsky, I. P. Wright, Magmatic carbon in Martian meteorites: Attempts to constrain the carbon cycle on Mars. *Int. J. Astrobiol.* **3**, 117–124 (1999).
7. A. Steele, F. M. McCubbin, M. D. Fries, The provenance, formation, and implications of reduced carbon phases in Martian meteorites. *Meteorit. Planet. Sci.* **51**, 2203–2225 (2016).
8. M. L. Fogel, A. Steele, Nitrogen in extraterrestrial environments: Clues to the possible presence of life. *Elements* **9**, 367–372 (2013).
9. H. C. Aoudjehane, G. Avice, J.-A. Barrat, O. Boudouma, G. Chen, M. J. M. Duke, I. A. Franchi, J. Gattacceca, M. M. Grady, R. C. Greenwood, C. D. K. Herd, R. Hewins, A. Jambon, B. Marty, P. Rochette, C. L. Smith, V. Sautter, A. Verchovsky, P. Weber, B. Zanda, Tissint martian meteorite: A fresh look at the interior, surface, and atmosphere of Mars. *Science* **338**, 785–788 (2012).
10. J. C. Bridges, M. M. Grady, A halite-siderite-anhydrite-chlorapatite assemblage in Nakhla: Mineralogical evidence for evaporites on Mars. *Meteorit. Planet. Sci.* **34**, 407–415 (1999).

11. P. Gillet, J. A. Barrat, P. Beck, B. Marty, R. C. Greenwood, I. A. Franchi, M. Bohn, J. Cotten, Petrology, geochemistry, and cosmic-ray exposure age of lherzolitic shergottite Northwest Africa 1950. *Meteorit. Planet. Sci.* **40**, 1175–1184 (2005).
12. H. G. Changela, J. C. Bridges, Alteration assemblages in the nakhlites: Variation with depth on Mars. *Meteorit. Planet. Sci.* **45**, 1847–1867 (2011).
13. L. J. Hicks, J. C. Bridges, S. J. Gurman, Ferric saponite and serpentine in the nakhlite martian meteorites. *Geochim. Cosmochim. Acta* **136**, 194–210 (2014).
14. P. Mane, R. Hervig, M. Wadhwa, L. A. J. Garvie, J. B. Balta, H. Y. McSween Jr., Hydrogen isotopic composition of the Martian mantle inferred from the newest Martian meteorite fall, Tissint. *Meteorit. Planet. Sci.* **51**, 2073–2091 (2016).
15. T. Mikouchi, Northwest Africa 1950: Mineralogy and comparison with Antarctic lherzolitic shergottites. *Meteorit. Planet. Sci.* **40**, 1621–1634 (2005).
16. T. E. Bunch, A. M. Reid, The Nakhlites Part I: Petrography and mineral chemistry. *Meteorit. Planet. Sci.* **10**, 303–315 (1975).
17. J. L. Gooding, M. E. Zolensky, S. J. Wentworth, Aqueous alteration of the Nakhla meteorite. *Meteoritics* **26**, 135–143 (1991).
18. J. C. Bridges, S. P. Schwenzer, The nakhlite hydrothermal brine on Mars. *Earth Planet. Sci. Lett.* **359–360**, 117–123 (2012).
19. Y. Chen, Y. Liu, Y. Guan, J. M. Eiler, C. Ma, G. R. Rossman, L. A. Taylor, Evidence in Tissint for recent subsurface water on Mars. *Earth Planet. Sci. Lett.* **425**, 55–63 (2015).
20. T. Usui, C. M. O. Alexander, J. Wang, J. I. Simon, J. H. Jones, Origin of water and mantle–crust interactions on Mars inferred from hydrogen isotopes and volatile element abundances of olivine-hosted melt inclusions of primitive shergottites. *Earth Planet. Sci. Lett.* **357–358**, 119–129 (2012).
21. L. J. Hallis, G. J. Taylor, K. Nagashima, G. R. Huss. Magmatic water in the martian meteorite Nakhla. *Earth Planet. Sci. Lett.* **359–360**, 84–92 (2012).
22. F. M. McCubbin, S. M. Elardo, C. K. Shearer Jr., A. Smirnov, E. H. Hauri, D. S. Draper, A petrogenetic model for the comagmatic origin of chassignites and nakhlites: Inferences from chlorine-rich minerals, petrology, and geochemistry. *Meteorit. Planet. Sci.* **48**, 819–853 (2013).
23. G. D. Cody, E. Heying, C. M. Alexander, L. R. Nittler, A. L. Kilcoyne, S. A. Sandford, R. M. Stroud, Establishing a molecular relationship between chondritic and cometary organic solids. *Proc. Natl. Acad. Sci. U.S.A.* **108**, 19171–19176 (2011).
24. A. W. Gillespie, F. L. Walley, R. E. Farrell, P. Leinweber, A. Schlichting, K.-U. Eckhardt, T. Z. Regier, R. I. R. Blyth, Profiling rhizosphere chemistry: Evidence from carbon and nitrogen K-edge XANES and pyrolysis-FIMS. *Soil Sci. Soc. Am. J.* **73**, 2002–2012 (2009).
25. H. Yabuta, M. Uesugi, H. Naraoka, M. Ito, A. L. D. Kilcoyne, S. A. Sandford, F. Kitajima, H. Mita, Y. Takano, T. Yada, Y. Karouji, Y. Ishibashi, T. Okada, M. Abe, X-ray absorption near edge structure spectroscopic study of Hayabusa category 3 carbonaceous particles. *Earth Planets Space* **66**, 156 (2014).
26. S. P. Kounaves, B. L. Carrier, G. D. O'Neil, S. T. Stroble, M. W. Claire, Evidence of martian perchlorate, chlorate, and nitrate in Mars meteorite EETA79001: Implications for oxidants and organics. *Icarus* **229**, 206–213 (2014).
27. M. H. Hecht, S. P. Kounaves, R. C. Quinn, S. J. West, S. M. M. Young, D. W. Ming, D. C. Catling, B. C. Clark, W. V. Boynton, J. Hoffman, L. P. Deflores, K. Gospodinova, J. Kapit, P. H. Smith, Detection of perchlorate and the soluble chemistry of martian soil at the Phoenix Lander site. *Science* **325**, 64–67 (2009).
28. M. R. Lee, T. Tomkinson, D. F. Mark, F. M. Stuart, C. L. Smith, Evidence for silicate dissolution on Mars from the Nakhla meteorite. *Meteorit. Planet. Sci.* **48**, 224–240 (2013).
29. M. Azuma, K. Hashimoto, M. Hiramoto, M. Watanabe, T. Sakata, Electrochemical reduction of carbon dioxide on various metal electrodes in low-temperature aqueous $KHCO_3$ media. *J. Electrochem. Soc.* **137**, 1772 (1990).
30. B. P. Sullivan, K. Krist, H. E. Guard, *Electrochemical and Electrocatalytic Reactions of Carbon Dioxide* (Elsevier, 2012).
31. J. Qiao, Y. Liu, J. Zhang, *Electrochemical Reduction of Carbon Dioxide* (CRC Press, 2016).
32. J. W. Halley, A. Schofield, B. Berntson, Use of magnetite as anode for electrolysis of water. *J. Appl. Phys.* **111**, 124911 (2012).
33. A. F. White, M. L. Peterson, M. F. Hochella Jr., Electrochemistry and dissolution kinetics of magnetite and ilmenite. *Geochim. Cosmochim. Acta* **58**, 1859–1875 (1994).
34. P. D. Allen, N. A. Hampson, G. J. Bignold, The effect of the potential on the dissolution of magnetite. *Surf. Technol.* **12**, 199–204 (1981).
35. G. H. Rau, S. A. Carroll, W. L. Bourcier, M. J. Singleton, M. M. Smith, R. D. Aines, Direct electrolytic dissolution of silicate minerals for air CO_2 mitigation and carbon-negative H_2 production. *Proc. Natl. Acad. Sci. U.S.A.* **110**, 10095–10100 (2013).
36. Y. Hori, Electrochemical CO_2 reduction on metal electrodes, in *Modern Aspects of Electrochemistry*, vol. 42 of *Modern Aspects of Electrochemistry*, C. G. Vayenas, R. E. White, M. E. Gamboa-Aldeco (Springer New York, 2008), pp. 89–189.
37. P. Zimmermann, C. Limberg, Activation of small molecules at nickel(I) moieties. *J. Am. Chem. Soc.* **139**, 4233–4242 (2017).
38. C. A. Paddon, M. Atobe, T. Fuchigami, P. He, P. Watts, S. J. Haswell, G. J. Pritchard, S. D. Bull, F. Marken, Towards paired and coupled electrode reactions for clean organic microreactor electrosyntheses. *J. Appl. Electrochem.* **36**, 617–634 (2006).
39. J. C. Stern, B. Sutter, C. Freissinet, R. Navarro-González, C. P. McKay, P. D. Archer Jr., A. Buch, A. E. Brunner, P. Coll, J. L. Eigenbrode, A. G. Fairen, H. B. Franz, D. P. Glavin, S. Kashyap, A. C. McAdam, D. W. Ming, A. Steele, C. Szopa, J. J. Wray, F. J. Martín-Torres, M. P. Zorzano, P. G. Conrad, P. R. Mahaffy; MSL Science Team, Evidence for indigenous nitrogen in sedimentary and aeolian deposits from the Curiosity rover investigations at Gale crater, Mars. *Proc. Natl. Acad. Sci. U.S.A.* **112**, 4245–4250 (2015).
40. Y. Abghoui, A. L. Garden, J. G. Howalt, T. Vegge, E. Skúlason, Electroreduction of N_2 to ammonia at ambient conditions on mononitrides of Zr, Nb, Cr, and V: A DFT guide for experiments. *ACS Catal.* **6**, 635–646 (2016).
41. J. A. Brandes, N. Z. Boctor, G. D. Cody, B. A. Cooper, R. M. Hazen, H. S. Yoder, Abiotic nitrogen reduction on the early Earth. *Nature* **395**, 365–367 (2013).
42. C.-X. Xiao, Z.-P. Cai, T. Wang, Y. Kou, N. Yan, Aqueous-phase Fischer–Tropsch synthesis with a ruthenium nanocluster catalyst. *Angew. Chem. Int. Ed. Engl.* **120**, 758–761 (2008).
43. J. P. Amend, E. L. Shock, Energetics of amino acid synthesis in hydrothermal ecosystems. *Science* **281**, 1659–1662 (1998).
44. T. M. McCollom, J. S. Seewald, Abiotic synthesis of organic compounds in deep-sea hydrothermal environments. *Chem. Rev.* **107**, 382–401 (2007).
45. M. D. Schulte, E. L. Shock, Thermodynamics of Strecker synthesis reactions during aqueous alteration of carbonaceous chondrite parent bodies. *Meteoritics* **27**, 286 (1992).
46. N. R. Lerner, E. Peterson, S. Chang, The Strecker synthesis as a source of amino acids in carbonaceous chondrites: Deuterium retention during synthesis. *Geochim. Cosmochim. Acta* **57**, 4713–4723 (1993).
47. S. L. Miller, H. C. Urey, Organic compound synthesis on the primitive earth. *Science* **130**, 245–251 (1959).
48. M. G. Vladimirov, Y. F. Ryzhkov, V. A. Alekseev, V. A. Bogdanovskaya, V. A. Otroshchenko, M. S. Kritsky, Electrochemical reduction of carbon dioxide on pyrite as a pathway for abiogenic formation of organic molecules. *Orig. Life Evol. Biosph.* **34**, 347–360 (2004).
49. T. M. McCollom, Laboratory simulations of abiotic hydrocarbon formation in Earth's deep subsurface. *Rev. Mineral. Geochem.* **75**, 467–494 (2013).
50. L. E. Mayhew, E. T. Ellison, T. M. McCollom, T. P. Trainor, A. S. Templeton, Hydrogen generation from low-temperature water–rock reactions. *Nat. Geosci.* **6**, 478–484 (2013).
51. R. W. Tock, W. A. Jackson, T. Anderson, S. Arunagiri, Electrochemical generation of perchlorate ions in chlorinated drinking water. *Corrosion* **60**, 757–763 (2004).
52. A. Jackson, S. Arunagiri, R. Tock, T. Anderson, K. Rainwater, Technical note: Electrochemical generation of perchlorate in municipal drinking water systems. *J. Am. Water Works Assoc.* **96** 103–108 (2004).
53. A. T. Kuhn, *Industrial Electrochemical Processes* (Elsevier Pub. Co., 1971).
54. M. Hayes, A. T. Kuhn, The preparation and behaviour of magnetite anodes. *J. Appl. Electrochem.* **8**, 327–332 (1978).
55. R. Domga, G. B. Noumi, J. B. Tchatchueng, Study of some electrolysis parameters for chlorine and hydrogen production using a new membrane electrolyzer. *Int. J. Chem. Eng. Anal. Sci.* **2**, 1–8 (2017).
56. C. R. Webster, P. R. Mahaffy, S. K. Atreya, G. J. Flesch, K. A. Farley; MSL Science Team, Low upper limit to methane abundance on Mars. *Science* **342**, 355–357 (2013).
57. R. Wirth. Focused Ion Beam (FIB) combined with SEM and TEM: Advanced analytical tools for studies of chemical composition, microstructure and crystal structure in geomaterials on a nanometre scale. *Chem. Geol.* **261**, 217–229 (2009).
58. R. Wirth. Focused ion beam (FIB): A novel technology for advanced application of micro- and nanoanalysis in geosciences and applied mineralogy. *Eur. J. Mineral.* **16**, 863–876 (2004).
59. E. H. Hauri, T. Weinreich, A. E. Saal, M. C. Rutherford, J. A. Van Orman, High pre-eruptive water contents preserved in lunar melt inclusions. *Science* **333**, 213–215 (2011).
60. A. Jull, J. W. Beck, G. S. Burr, Isotopic evidence for extraterrestrial organic material in the Martian meteorite, Nakhla. *Geochim. Cosmochim. Acta* **64**, 3763–3772 (2000).
61. S. Siljeström, M. N. Parenteau, L. L. Jahnke, S. L. Cady, A comparative ToF-SIMS and GC–MS analysis of phototrophic communities collected from an alkaline silica-depositing hot spring. *Org. Geochem.* **109**, 14–30 (2017).
62. E. L. Walton, C. D. K. Herd, Localized shock melting in lherzolitic shergottite Northwest Africa 1950: Comparison with Allan Hills 77005. *Meteorit. Planet. Sci.* **42**, 63–80 (2007).
63. J. Fritz, N. Artemieva, A. Greshake, Ejection of Martian meteorites. *Meteorit. Planet. Sci.* **40**, 1393–1411 (2005).
64. I. P. Baziotis, Y. Liu, P. S. DeCarli, H. J. Melosh, H. Y. McSween, R. J. Bodnar, L. A. Taylor, The Tissint Martian meteorite as evidence for the largest impact excavation. *Nat. Commun.* **4**, 1404 (2013).
65. B. P. Weiss, H. Vali, F. J. Baudenbacher, J. L. Kirschvink, S. T. Stewart, D. L. Shuster, Records of an ancient Martian magnetic field in ALH84001. *Earth Planet. Sci. Lett.* **201**, 449–463 (2002).

66. D. Stoffler, *Deformation and Transformation of Rock-Forming Minerals by Natural and Experimental Shock Processes: II. Physical Properties of Shocked Minerals* (Fortschritte der Mineralogie, 1974), vol. 51.
67. A. Steele, M. D. Fries, H. E. F. Amundsen, B. O. Mysen, M. L. Fogel, M. Schweizer, N. Z. Boctor, Comprehensive imaging and Raman spectroscopy of carbonate globules from Martian meteorite ALH 84001 and a terrestrial analogue from Svalbard. *Meteorit. Planet. Sci.* **42**, 1549–1566 (2007).
68. P. A. Bland, G. S. Collins, T. M. Davison, N. M. Abreu, F. J. Ciesla, A. R. Muxworthy, J. Moore, Pressure-temperature evolution of primordial solar system solids during impact-induced compaction. *Nat. Commun.* **5**, 5451 (2014).

Acknowledgments: This paper is dedicated to the memory of Erik Hauri. Rock in peace. A.S. acknowledges M. Glamoclija and the Carnegie Institution of Washington. We thank C. Smith of the Natural History Museum in London for providing samples of the Tissint meteorite. We thank J. Jensen at Linköping University for help with ToF-SIMS analyses. L.G.B. acknowledges the help of M. Ward for some of the TEM work done at the LEMAS center at the University of Leeds. We thank the reviewers of this paper for their helpful and insightful comments that improved the quality of the manuscript. **Funding:** A.S. acknowledges funding from NASA grants NNX13AJ19G (A.St., principal investigator) and NNX14AT28G (M. Glamoclija, principal investigator). S.S. was funded by the Swedish National Space Board (contracts 121/11 and 198/15), the Swedish Research Council (contract 2015-04129), and the DCO. L.G.B. acknowledges financial support from the Helmholtz Recruiting Initiative (award number I-044-16-01). The ALS was supported by the Director, Office of Science, Office of Basic Energy Sciences, of the U.S. Department of Energy under contract no. DE-AC02-05CH11231. **Author contributions:** A.S. conceived and planned the study; performed instrument analysis, data reduction, and data interpretation; and wrote the paper. S.S., A.N., R.W., A. Schreiber, L.G.B., D.K., J.H.W., E.H., and J.D.R.B. performed data acquisition and/or analysis. F.M.M., M.D.F., and K.R. interpreted and discussed data. All authors contributed to the writing of the paper. **Competing interests:** The authors declare that they have no competing interests. **Data and materials availability:** All data needed to evaluate the conclusions in the paper are present in the paper and/or the Supplementary Materials. Additional data related to this paper may be requested from the authors.

Submitted 6 March 2018
Accepted 25 September 2018
Published 31 October 2018
10.1126/sciadv.aat5118

Citation: A. Steele, L. G. Benning, R. Wirth, S. Siljeström, M. D. Fries, E. Hauri, P. G. Conrad, K. Rogers, J. Eigenbrode, A. Schreiber, A. Needham, J. H. Wang, F. M. McCubbin, D. Kilcoyne, J. D. Rodriguez Blanco, Organic synthesis on Mars by electrochemical reduction of CO_2. *Sci. Adv.* **4**, eaat5118 (2018).